Inversion of Dielectric Properties of the Lunar Regolith Media With Temperature Profiles Using Chang'e Microwave Radiometer Observations

Xiaohui Gong, David A. Paige, Matthew A. Siegler, and Ya-Qiu Jin, *Fellow, IEEE*

***Abstract*—As ground truth to utilize the surface temperature measurements from the Diviner Lunar IR Radiometer and the subsurface thermal properties from the Apollo heat-flow probes, we create a forward model to predict brightness temperatures (Tbs) from lunar regolith media in the microwave (MW) spectrum. These models can be then directly compared with and matched to the data from the MW radiometers flown aboard the Chang'e 1 and 2 (CE-1 and CE-2) missions. Based on an MW radiative transfer model and the least-mean-square method, the effective surface reflectivity and absorption coefficient of the lunar regolith are retrieved from multichannel MW Tbs. The effective complex dielectric constant of the lunar regolith as a function of the depth at different frequency channels is derived. Meanwhile, we find that the maximum penetration depth of the MW radiation at the Apollo 15 site ranges from about 30 cm at 37.0 GHz to 230 cm at 3.0 GHz and from 30 cm at 37.0 GHz to 560 cm at 3.0 GHz in the equatorial highlands, which are much lower than the previous results that were simply derived from FeO and TiO_2 abundance.**

***Index Terms*—Apollo heat flow, brightness temperature (Tb), Chang'e 1 and 2 (CE-1 and CE-2), dielectric properties, Diviner, radiative transfer, regolith media, temperature profile.**

I. Introduction

STUDIES of the lunar regolith layer might provide the physical and structural information of mineral deposits formed during the lunar evolutionary history. A key parameter is the dielectric constant of regolith media. The dielectric constant at microwave (MW) frequencies had been generally only estimated from the FeO and TiO_2 abundance from Apollo limited samples and from spectral albedo measurements [13], [8]–[10]. However, the samples from a location were very limited, and the spectral albedo measurement only based on the optical reflectivities of the FeO and TiO_2 components largely restricted the accuracy of calibration. In addition, these approaches do not take account of other factors that might influence the effective dielectric constants in multichannel remote observations and the topography of a cratered rough surface or other mineral compounds.

Manuscript received June 25, 2014; accepted July 24, 2014. Date of publication August 15, 2014; date of current version August 21, 2014. *(Corresponding author: Ya-Qiu Jin.)*

X. Gong and Y.-Q. Jin are with the Key Laboratory for Information Science of Electromagnetic Waves, Ministry of Education, Fudan University, Shanghai 200433, China (e-mail: yqjin@fudan.edu.cn).

D. A. Paige is with the Department of Earth and Space Sciences, University of California Los Angeles, Los Angeles, CA 90095-1567 USA.

M. A. Siegler is with the Jet Propulsion Laboratory, California Institute of Technology, Pasadena, CA 91109 USA.

Color versions of one or more of the figures in this paper are available online at http://ieeexplore.ieee.org.

Digital Object Identifier 10.1109/LGRS.2014.2343617

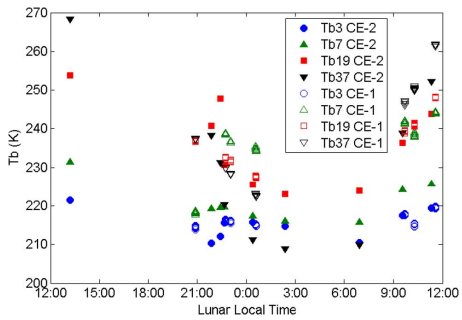

Fig. 1. Multichannel Tb data of CE-1 and CE-2 at different lunar local times at the Apollo 15 site.

Because of almost no penetration, Diviner IR measurements actually presented the surface physical temperature, whereas the MW can penetrate into the regolith media, and the MW radiometer can present the MW emission from the whole penetrated media. In this letter, we use independent Diviner IR measurements of the surface temperature and the regolith density in literature [6] to fuse the Chinese Chang'e 1 and 2 (CE-1 and CE-2) MW multichannel radiometer observations, and the numerical results of the radiative transfer modeling with these multichannel MW emissions are employed to estimate the effective dielectric constants of global regolith media in multifrequencies. The analysis of the examples is particularly performed at the Apollo 15 site and in a broad region of the equatorial lunar highlands.

II. CE-1 and CE-2 MW Tb Observations at Apollo 15 Site

In 2007 and 2010, China successfully launched its first lunar satellites, i.e., CE-1 and CE-2. The payloads for both spacecraft included the CE multichannel MW radiometers, which obtained thermal emission measurements in four spectral channels centered on 3.0, 7.8, 19.35, and 37.0 GHz at a spatial resolution of $\sim$50 km. These are the first global measurements of the Moon at these wavelengths [2], [4].

The CE MW brightness temperature (Tb) data at the Apollo 15 site within a $1^\circ \times 1^\circ$ box centered at (26.4 °N, 3.65 °E) were collected. CE-1 obtained 1307 tracks across this region from November 2008 to February 2009 and from May 2009 to July 2009. CE-2 obtained 1468 tracks across this region from October 2010 to February 2011. The lunar local time of each observation was calculated following the literature [3].

Fig. 1 shows the CE MW Tb data at different lunar local times at the Apollo 15 site. In total, 75 tracks of CE-1 data at seven different local times and 61 tracks of CE-2 data at nine different local times were collected.

By comparing the CE-1 and CE-2 data, it can be seen that the observations at high-frequency channels, e.g., 37.0 and 19.35 GHz, and the lowest frequency channel at 3 GHz are quite consistent within few kelvin differences. However, the CE-2 Tb data at the 7.8-GHz channel seem much lower, e.g., 20 K, than CE-1. We attribute this inconsistency to a hardware or calibration problem.

III. Lunar Regolith Temperature and Density Profiles at Apollo 15 Site

The heat-flow experiment at the Apollo 15 site may provide us with the physical temperatures of the surface and subsurface media [7]. These results were introduced to fit by thermal models [6], and the resulting surface temperature had been directly validated by the IR observations of the Lunar Reconnaissance Orbiter Diviner radiometer [15]. Diviner has seven IR channels with three spectral filters near the 8-μm wavelength and four separate channels covering 12–25, 25–50, 50–100, and 100–300 μm, respectively [12].

Under direct solar insolation, the lunar surface temperature is governed by solar illumination at daytime, and it is dominated by thermal conduction during nighttime. Generally, the regolith media form a nonuniform temperature profile $T(z)$ and bulk density profile $\rho(z)$ during a long evolution history. In a layered media model of regolith and bedrock [11], [14], the lunar regolith was taken as a 2-cm top-dust layer and a more conductive and compacted regolith layer. By analyzing the heat-flow experiment at the Apollo 15 site, Keihm [6] gave a bulk density $\rho(z)$ as

$$\begin{aligned}\rho(z) &= 1.25, \quad \text{as } z \le 2 \text{ cm} \\ \rho(z) &= 1.25 + 0.65 \times \left[1 - e^{\frac{-(z-2)}{4}}\right], \quad \text{as } z > 2 \text{ cm}. \end{aligned} \tag{1}$$

If only the solid thermal conductivity and radiation in the regolith are taken into account and other radiations from the background and the radioactive origin are neglected, the 1-D thermal diffusion equation is well applied to solve temperature $T(z)$ as follows:

$$\frac{\partial}{\partial z}\left(K(z,T)\frac{\partial T}{\partial z}\right) = \rho(z)C(T)\frac{\partial T}{\partial t} + J(z) \tag{2}$$

where $K(z, T)$ is the thermal conductivity at depth z and temperature T, C is the specific heat capacity, and t is the time. $J(z)$ indicates the influence of the internal heat flow, which is usually very small to be ignored. Under two conditions, i.e., the increased or decreased energy in each layer satisfies the energy conservation law and the temperature achieved thermal balance at a deep depth, (2) for each lunar local time can be solved using the finite-difference time-domain method.

Following Keihm's analysis [6], we obtained the physical temperature profile $T(z)$ at the Apollo 15 site for the lunar local time. Fig. 2 shows the calculated surface temperatures compared with the Diviner IR channel 7 Tb measurements. A large variation in the surface diurnal temperature can be seen, and a dashed line is indicated as the nearly constant temperature at a depth of approximately 25 cm below the surface.

Fig. 3 shows the temperature profiles at the Apollo 15 site calculated at different lunar local times. It is shown that there are large diurnal variations in the temperature of the upper regolith media. For example, a surface temperature of 380 K at daytime can be cooled to 100 K at nighttime. The temperature becomes constant around a depth of 25 cm.

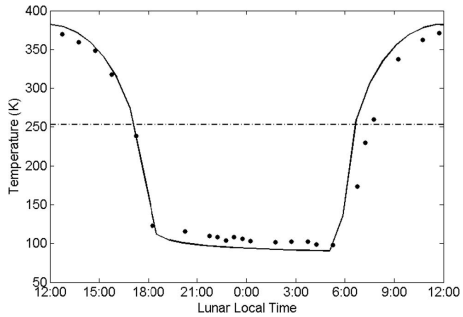

Fig. 2. Model-calculated surface temperature variations at the Apollo 15 site (line) validated by the Diviner IR data at the Apollo 15 site (dots).

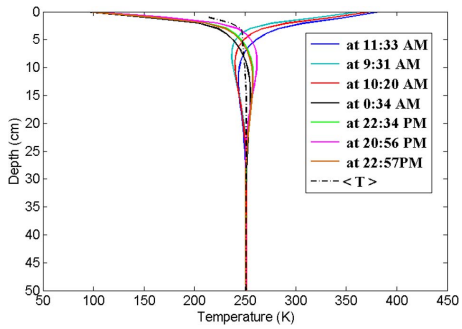

Fig. 3. Calculated temperature profiles at different local times at the Apollo 15 site.

IV. Inversion of Dielectric Constant From CE-1 and CE-2 Tb Data at Apollo 15 Site

Assuming the regolith is a half-space ($z \in [0, \infty]$) with a temperature profile $T(z)$, the observed Tb can be calculated by the Wentzel–Kramers–Brillouin (WKB) solution for an inhomogeneous medium with sufficiently small spatial variation of the MW radiative transfer [5] as follows (where an observation angle of 0° is taken as the CE radiometer system):

$$T_{Bv} = (1 - r_v)\int_0^\infty \rho(z)\kappa_v(z)T(z)e^{-\int_0^z \rho(z')\kappa_v(z')dz'}dz \tag{3}$$

where r_ν is the surface reflectivity at frequency v, and $\kappa_\nu(z)$ is the absorption coefficient that is mainly governed by the imagery part of dielectric constant ε''. Note that κ_ν can be seen as a constant because the nonuniform bulk density profile $\rho(z)$ has been taken into account. The reflections between inhomogeneous layers are usually neglected in the WKB solution. Equation (3) is usually applied to the inhomogeneous media with a flat surface, but it may be also employed to the model with a gently rough surface with zeroth-order approximated r_ν.

There are two unknowns, i.e., r_ν and κ_ν, in (2). Using the Tb data from CE-1 and CE-2 and the validated temperature profiles at the lunar local time, an approach to find the best fit values of r_ν and κ_ν can be obtained based on the least square method as follows:

$$\Delta = \min \sum \sqrt{(T_{b\nu} - \tilde{T}_{b\nu})^2}. \tag{4}$$

Iteratively testing r_ν with a range of (0.01–0.2) and, correspondingly, κ_ν/f with a range of (0.8×10^{-10}–3.0×10^{-10}),

TABLE I
BEST FIT PARAMETERS FROM THE CE-1 MW TB AT THE APOLLO 15 SITE

Channel (Ghz)	λ (cm)	r_ν	κ_ν / f (m·g/cm^3·Hz)$^{-1}$	κ_ν (m·g/cm^3)$^{-1}$	$d_{\max}$ (cm)	$d_{\min}$ (cm)	ε'	$\tan\delta/\rho$
37	0.8108	0.0300	1.2×10^{-10}	4.4400	36.04	23.71	2.012	0.0041
19	1.5504	0.0500	1.1×10^{-10}	2.1285	75.17	49.46	2.482	0.0034
7	3.8462	0.0425	1.6×10^{-10}	1.2480	128.21	84.36	2.307	0.0050
3	10.000	0.1345	2.3×10^{-10}	0.6900	231.88	152.58	4.656	0.0051

TABLE II
BEST FIT PARAMETERS FROM THE CE-2 MW TB AT THE APOLLO 15 SITE

Channel (Ghz)	λ (cm)	r	κ_ν / f (m·g/cm^3·Hz)$^{-1}$	κ_ν (m·g/cm^3)$^{-1}$	$d_{\max}$ (cm)	$d_{\min}$ (cm)	ε'	$\tan\delta/\rho$
37	0.8108	0.0650	1.6×10^{-10}	5.9200	27.03	17.78	2.835	0.0045
19	1.5504	0.0600	1.4×10^{-10}	2.7090	59.06	38.86	2.717	0.0041
7	3.8462	0.1100	2.15×10^{-10}	1.6770	95.41	62.78	3.968	0.0052
3	10.000	0.1350	2.6×10^{-10}	0.7800	205.13	134.98	4.670	0.0057

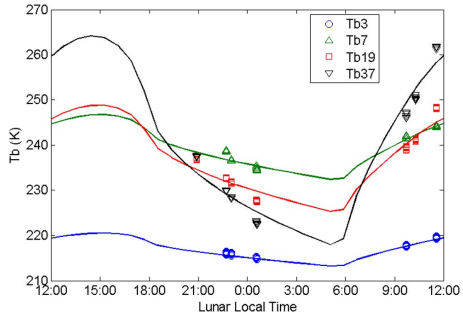

Fig. 4. Comparison of the diurnal MW Tb for each channel with the CE-1 data at the Apolo 15 site.

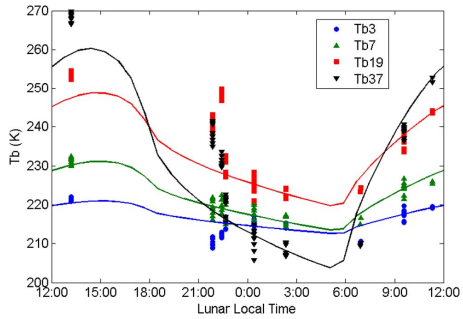

Fig. 5. Comparison of the diurnal MW Tb for each channel with the CE-2 data at the Apolo 15 site.

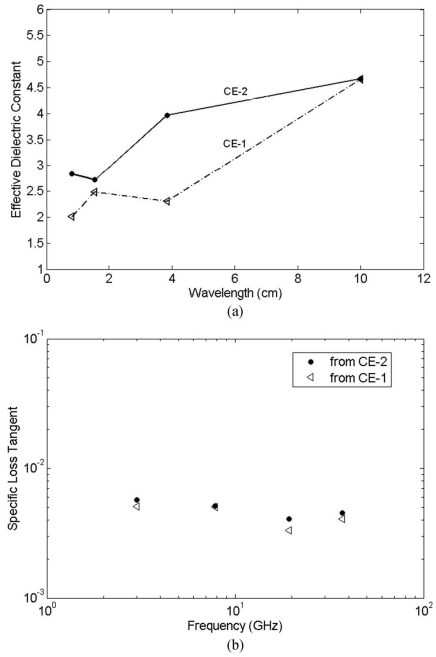

Fig. 6. Effective complex dielectric constant inverted from the CE-1 and CE-2 MW Tb data at the Apolo 15 site. (a) Real part of the effective dielectric constant for different channels. (b) Imaginary part, i.e., the specific loss tangent, of the effective dielectric constant for different channels.

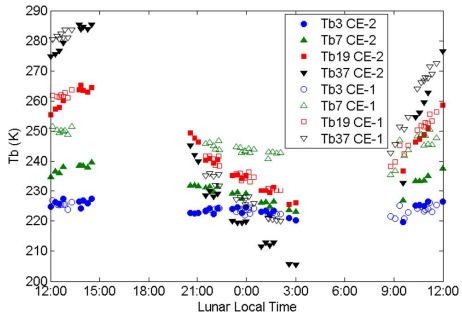

Fig. 7. MW Tb data of CE-1 and CE-2 at different lunar local times around the equatorial highlands.

the best fit parameters can be obtained, as shown in Tables I and II for the CE-1 and CE-2 data, respectively.

As r_ν is obtained, we can have the real part of the effective dielectric constant of the medium, i.e., ε'_ν, in the calculation of $r_\nu = |(1-\sqrt{\varepsilon'})/(1+\sqrt{\varepsilon'})|^2$ under the 0° observation [5]. Moreover, using κ_ν and ε'_ν, we obtain the imaginary part of effective dielectric constant $\varepsilon''_\nu = \kappa_\nu \overline{\rho} c\sqrt{\varepsilon'_\nu}/(2\pi f)$, where $\overline{\rho}$ is the average number of $\rho(z)$ over z. We take $\overline{\rho} = 1.25$ from (1) to make the minimum of ε''_ν. Note that penetration depth d is defined as $e^{-k''d} \equiv e^{-1}$, where $k'' = \kappa_\nu \overline{\rho}/2$ is the imaginary part of the complex wavenumber of the medium. Then, we can have the maximum penetration depth, i.e., $d_{\max} = 2/(\kappa_\nu \overline{\rho})$, as listed in Tables I and II. If $\overline{\rho} = 1.9$ is taken, it may yield the minimum of the penetration depth, i.e., $d_{\min}(1.25/1.9)d_{\max}$.

In these tables, it is shown that reflectivity r_ν increases and κ_ν decreases as the wavelength increases, whereas κ_ν/f remains stable. The results with the data recorded at 37.0, 19.35, and 3.0 GHz from CE-1 and CE-2 are well consistent, excluding the 7.8-GHz channel.

TABLE III
BEST FIT PARAMETERS AND DIELECTRIC CONSTANT OF THE EQUATORIAL HIGHLANDS FROM THE CE-1 DATA

Channel (Ghz)	λ (cm)	r	κ_ν / f (m·g/cm^3·Hz)$^{-1}$	κ_ν (m·g/cm^3)$^{-1}$	$d_{\max}$ (cm)	$d_{\min}$ (cm)	ε'	$\tan\delta/\rho$
37	0.8108	0.0450	1.2×10^{-10}	4.4400	34.65	23.71	2.365	0.0039
19	1.5504	0.0650	1.1×10^{-10}	2.1285	72.28	49.45	2.835	0.0032
7	3.8462	0.0550	0.6×10^{-10}	0.4680	328.73	224.92	2.599	0.0018
3	10.000	0.0600	0.85×10^{-10}	0.2550	603.32	412.80	2.717	0.0024

TABLE IV
BEST FIT PARAMETERS AND DIELECTRIC CONSTANT OF THE EQUATORIAL HIGHLANDS FROM THE CE-2 DATA

Channel (Ghz)	λ (cm)	r	κ_ν / f (m·g/cm^3·Hz)$^{-1}$	κ_ν (m·g/cm^3)$^{-1}$	$d_{\max}$ (cm)	$d_{\min}$ (cm)	ε'	$\tan\delta/\rho$
37	0.8108	0.0650	1.35×10^{-10}	4.9950	30.80	21.07	2.835	0.0038
19	1.5504	0.0700	1.05×10^{-10}	2.0310	75.75	51.83	2.955	0.0029
7	3.8462	0.1200	1.00×10^{-10}	0.7800	197.24	134.95	4.241	0.0023
3	10.000	0.0710	0.9×10^{-10}	0.2700	569.80	389.86	2.979	0.0025

Using these inverted best fit parameters and the temperature profiles, the diurnal variation in the Tb can be calculated. Figs. 4 and 5 present the comparison between the simulated diurnal Tb (curve) and the observed diurnal Tb (discrete dots) from CE-1 and CE-2 at the Apollo 15 site, respectively. It is shown that the simulation of diurnal variations well matches the actual Tb data at different local times.

Fig. 6 gives the inverted ε'_ν and $\tan\delta$ for each channel. They are termed effective because of the assumptions used in our model. The results demonstrate that different frequencies can see different depths of the media and yield different, i.e., effective, dielectric constants. Lower frequencies have a larger penetration depth, and as a result, its effective dielectric constant can get more weight from deeper media, and vice versa.

Following (1), suppose that the dielectric constant of the top-dust layer with a depthd_1 is ε_{10} and that the dielectric constant of the underlying regolith media is $\varepsilon(z)$, which is written as

$$\varepsilon(z) = \varepsilon_{10} + (\varepsilon_{20} - \varepsilon_{10})\left(1 - e^{-\alpha(z-d_1)}\right), \quad z > d_1 \tag{5}$$

where ε_{20} represents the dielectric constant when $z \to \infty$, and α can be viewed as an attenuation factor. From the wave propagation, the phase term is written as

$$k_{\text{eff}} Z = k_0\sqrt{\varepsilon_{10}}d_1 + \int_{d_1}^{Z} dz k_0 \sqrt{\varepsilon_{10} + (\varepsilon_{20} - \varepsilon_{10})\left(1 - e^{-\alpha(z-d_1)}\right)} \tag{6}$$

where Z is simply a depth for accounting the phase term in propagation. It yields

$$\sqrt{\varepsilon_{\text{eff}}} \sim \sqrt{\varepsilon_{10}}\frac{d_1}{Z} + \sqrt{\varepsilon_{10}}\left[\left(1 - \frac{d_1}{Z}\right)\frac{\varepsilon_{20} + \varepsilon_{10}}{2\varepsilon_{10}} + \frac{\varepsilon_{20} - \varepsilon_{10}}{2\varepsilon_{10}\alpha Z}\left(e^{-\alpha(Z-d_1)} - 1\right)\right]. \tag{7}$$

It can be seen that $\sqrt{\varepsilon_{\text{eff}}} \sim \sqrt{\varepsilon_{10}}$ when $Z \sim d_1$ for the high-frequency channels with poor penetration ability, and only the shallow surface layer can be detected. When $Z \gg d_1$, as the depth increases, it has $\sqrt{\varepsilon_{\text{eff}}} \propto \sqrt{\varepsilon_{20}}$ at the low-frequency channels with high penetration ability. Thus, it is quite reasonable that the inverted effective dielectric constants are related to the frequency.

V. INVERSION OF DIELECTRIC CONSTANT FROM CE-1 AND CE-2 TB AT EQUATORIAL HIGHLANDS

We treat the Moon's equatorial highlands as one region for inverting the dielectric constant since the equatorial highlands' regolith should have similar mineral composition and physical properties. Vasavada *et al.* [15] studied the thermal model and the surface temperature with validation from the Diviner IR data. Using the same approach, the physical temperature profiles $T(z)$ at the equatorial highlands are applied to the inversions of parameters r_ν and κ_ν. The equatorial highlands are chosen as a belt within the latitudes of $\pm0.5^\circ$ and longitudes from -180° to -75° and from 100° to 180°.

Fig. 7 shows the Tb data from CE-1 and CE-2 at different local times around the equatorial highlands. These data have been averaged every 15 min, yielding a total of 40 observations from CE-1 and 32 observations from CE-2.

Based on the work in [14], it takes $\overline{\rho} = 1.3$. The best fit parameters and inverted dielectric constant of the equatorial highlands from the CE-1 and CE-2 Tb data are given in Tables III and IV, respectively.

As a comparison with Tables I and II, the penetration depth of the 3.0-GHz channel at the equatorial highlands is about 3 times deeper than that at the Apollo 15 site. The deeper penetration may be explained as the decreased abundance of FeO and TiO_2 at the equatorial highlands, which, in turn, lowered the loss tangent.

Based on these parameters and the physical temperature profiles at different local times, the diurnal variation in the Tb at the equatorial highlands can be calculated from (2). Figs. 8 and 9 present these simulated Tbs and the CE-1 and CE-2 data at different local times and for different channels. It is shown that the diurnal Tb variation of the high-frequency channel is much more dramatic than that of the low-frequency channel because the Tb of the high-frequency channel is more sensitive to the diurnal variation in the surface temperature, and vice versa.

Fig. 10 gives the effective dielectric constants inverted for all the channels at the equatorial highlands. Compared with the dielectric constants retrieved for the Apollo 15 site, the effective dielectric constants seem similar for the high-frequency channels (19.35 and 37.0 GHz), but they become much lower at the low-frequency channels (3.0 GHz). In particular, the loss tangent is lower than the results from the maria of the

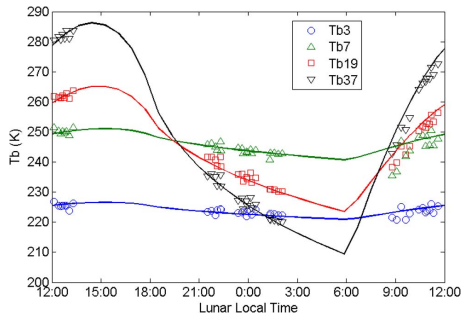

Fig. 8. Comparison between the Tb simulation and the CE-1 data at the equatorial highlands.

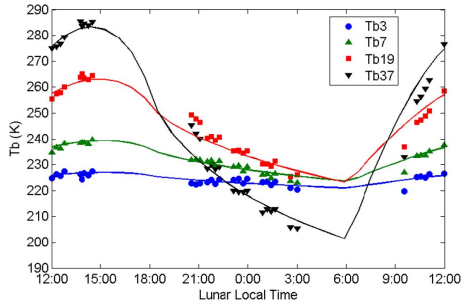

Fig. 9. Comparison between the Tb simulation and the CE-2 data at the equatorial highlands.

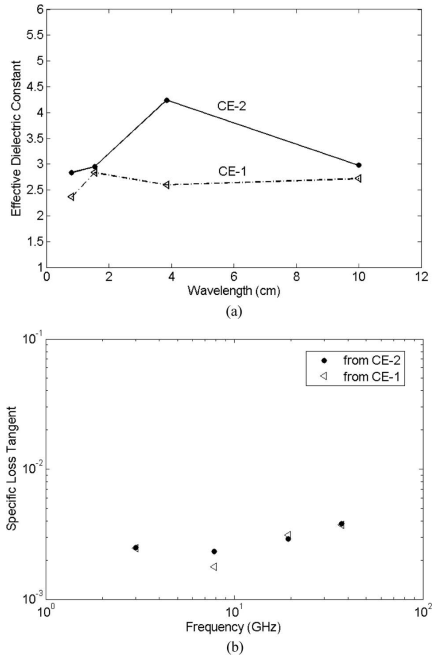

Fig. 10. Effective complex dielectric constant inverted from the CE-1 and CE-2 Tb data at the equatorial highlands. (a) Real part of the effective dielectric constant. (b) Imaginary part, i.e., the specific loss tangent, of the effective dielectric constant.

Apollo 15 site. This result also agrees with the decreased abundance of FeO and TiO_2 at the equatorial highlands, which might cause lower reflectivity and higher emissivity.

VI. Conclusion

Using the solutions of the 1-D thermal diffusion equation, the temperature profiles at different lunar local times can be obtained and then validated by the Diviner IR data. Based on the parameters and temperature profiles, the CE-1 and CE-2 multichannel MW Tb data are applied to invert the best fitted reflectivity and absorption coefficient of the regolith media based on the WKB solution of the radiative transfer model. It gives the inverted effective complex dielectric constant of the regolith media.

Two examples, i.e., the Apollo 15 site maria and the equatorial highlands, have been chosen for this letter. A large amount of MW Tb data from both CE-1 and CE-2 are collected and applied to the inversions. The diurnal variations in the MW Tb are also simulated based on the inverted parameters and temperature profiles. These Tb simulations of all four channels and its diurnal variations are well matched with the observations from CE-1 and CE-2 correspondingly. Different penetration depths for different frequencies indicate that the inverted effective dielectric constant is dependent on the frequency of observation. It is also related to the bulk density profile, the abundance of FeO and TiO_2, etc. The inverted results from the CE data show that the penetration ability of the MW is lower than that only predicted from the FeO and TiO_2 content in previous studies. The results of this letter have demonstrated the utility of the CE MW data in conjunction with independently derived soil temperatures for determining the dielectric constants of lunar soil. In the future, the results of this letter can be extended to create global-scale maps of lunar soil dielectric constants.

References

[1] J. N. Cuzzi and D. O. Muhleman, "The microwave spectrum and nature of the subsurface of mars," *Icarus*, vol. 17, no. 2, pp. 548–560, Mar. 1972.

[2] W. Fa and Y. Q. Jin, "A primary analysis of microwave brightness temperature of lunar surface and Chang-E 1 multi-channel radiometer observation and inversion of regolith layer thickness," *Icarus*, vol. 207, no. 2, pp. 605–615, Jun. 2010.

[3] X. Gong and Y. Q. Jin, "Diurnal physical temperature at Sinus Iridum area retrieved from observations of Chinese Chang'E-1 microwave radiometer," *Icarus*, vol. 218, no. 2, pp. 807–816, Apr. 2012.

[4] J. S. Jiang and Y. Q. Jin, *Selected Papers on Microwave Lunar Exploration in Chinese Chang'E-1 Project*. Beijing, China: Science Press, 2011.

[5] Y. Q. Jin, *Electromagnetic Scattering Modelling for Quantitative Remote Sensing*. Singapore: World Scientific, 1994.

[6] S. J. Keihm, "Interpretation of the lunar microwave brightness temperature spectrum: Feasibility of orbital heat flow mapping," *Icarus*, vol. 60, no. 3, pp. 568–589, Dec. 1984.

[7] M. G. Langseth, S. J. Keihm, and K. Peters, "Revised Lunar Heat-Flow Values," in *Proc. Lunar Planetary Sci. Conf.*, 1976, vol. 7, pp. 3143–3171.

[8] P. G. Lucey, G. J. Taylor, and E. Malaret, "Abundance and distribution of iron on the Moon," *Science*, vol. 268, no. 5214, pp. 1855–1858, May 1995.

[9] P. G. Lucey, D. T. Blewett, and B. R. Hawke, "Mapping the FeO and TiO2 content of the lunar surface with multispectral imagery," *J. Geophys. Res.*, vol. 103, no. E2, pp. 3679–3699, Feb. 1998.

[10] P. G. Lucey, D. T. Blewett, and B. L. Jolliff, "Lunar iron and titanium abundance algorithms based on final processing of Clementine ultraviolet—Visible images," *J. Geophys. Res., Planets (1991–2012)*, vol. 105, no. E8, pp. 20297–20305, Aug. 2000.

[11] D. L. Mitchell and I. D. Pater, "Microwave imaging of Mercury's thermal emission at wavelengths from 0.3 to 20.5 cm," *Icarus*, vol. 110, no. 1, pp. 2–32, Jul. 1994.

[12] D. A. Paige *et al.*, "The Lunar Reconnaissance Orbiter Diviner lunar radiometer experiment," *Space Sci. Rev.*, vol. 150, no. 1–4, pp. 125–160, Jan. 2010.

[13] Y. G. Shkuratov, V. G. Kaydash, and N. V. Opanasenko, "Iron and titanium abundance and maturity degree distribution on the lunar nearside," *Icarus*, vol. 137, no. 2, pp. 222–234, Feb. 1999.

[14] A. R. Vasavada, D. A. Paige, and S. E. Wood, "Near-surface temperatures on Mercury and the Moon and the stability of polar ice deposits," *Icarus*, vol. 141, no. 2, pp. 179–193, Oct. 1999.

[15] A. R. Vasavada *et al.*, "Lunar equatorial surface temperatures and regolith properties from the Diviner Lunar Radiometer Experiment," *J. Geophys. Res., Planets (1991–2012)*, vol. 117, no. E4, pp. E00H18-1–E00H18-12, Dec. 2012.